



A large acceptance spectrometer for the internal target facility at NIKHEF

D.J.J. de Lange^a, J.J.M. Steijger^{a,*}, H. de Vries^a, M. Anghinolfi^b, M. Taiuti^b,
D.W. Higinbotham^c, B.E. Norum^c, E. Konstantinov^d

^a NIKHEF, P.O. Box 41882 1009 DB Amsterdam, The Netherlands

^b Istituto Nazionale di Fisica Nucleare and Dipartimento di Fisica, via Dodecaneso 33, 16146 Genova, Italy

^c University of Virginia, Charlottesville, VA 22901, USA

^d Budker Institute for Nuclear Physics, Novosibirsk 630090, Russian Federation

Received 31 October 1997

Abstract

A non-focusing magnetic spectrometer, BigBite, has been built for use at the Internal Target Facility of the AMP ring at NIKHEF. It allows detection of particles with momentum in the range of 200–900 MeV/c, with an angular resolution of about 4 mrad, and a design momentum resolution of 5×10^{-3} . The track of a particle after passage through the field of a single dipole magnet is determined by two multi-wire drift chambers each of which has two planes. The four planes contain a total of 338 sense wires. For each plane, both sense wires and cathode strips are used to make measurements of each coordinate. The trigger consists of coincident signals from a single scintillator and a diffusely reflecting aerogel Cherenkov detector. The latter also provides discrimination between electrons and pions. Details of the signal handling and first results on the performance of the complete system will be discussed. © 1998 Elsevier Science B.V. All rights reserved.

PACS: 29.30.Aj; 29.40.Gx; 29.40; Ka 29.40.Mc

Keywords: Electron spectrometer; Magnetic spectrometer; Drift chambers; Electron scattering; Cherenkov detector

1. Introduction

In nuclear physics experiments with electron beams one of the most important kinematical variables is the momentum q transferred by the virtual photon. It is necessary to determine the energy and

direction of the scattered electron to obtain q . This can be considered as tagging the virtual photon.

At many facilities focusing magnetic spectrometers are used for this purpose. These instruments combine good angular resolution with good momentum resolution. In internal target experiments storage cells are commonly used [1–3] to obtain a sufficiently high target thickness. Typically, these targets extend some 40 cm along the beam line. Many focusing spectrometers cannot accept this

* Corresponding author. Tel.: + 31 20 592 2076; fax: + 31 20 592 5155; e-mail: josst@nikhef.nl.

range. Furthermore, the small momentum acceptance (around 10%) and the small solid angle (typically 5–10 msr) of these spectrometers are insufficient to deal with the small yield from the low luminosity that can be achieved with polarized targets.

Larger acceptances can be obtained with non-magnetic detectors. The energy resolution of such devices for electrons below 1 GeV, however, is not better than 10% [4,5]. This resolution is insufficient for a general-purpose electron spectrometer.

We have chosen to build a non-focusing magnetic spectrometer. This solution combines a large angular acceptance (almost 100 msr) with a large momentum acceptance (particles with a momentum between 200 and 900 MeV/c are accepted). The instrument can detect electrons from extended targets with a length of ± 10 cm projected on the direction perpendicular to the symmetry plane of the magnet.

In Section 2 some design considerations are given. Section 3 describes the magnet and its support structure. In Section 4 the detector system is set out. Section 5 describes the data acquisition. In Section 6 the results obtained in test measurements are discussed.

2. Design specifications

As discussed in the previous section we have chosen to use a non-focusing magnetic spectrometer. The required resolution of this spectrometer is given by the precision with which q should be known ($dq \leq 2$ MeV/c), and the equation defining the momentum transfer

$$q = \sqrt{p_e^2 + p_{e'}^2 - 2p_e p_{e'} \cos \theta}, \quad (1)$$

where θ is the scattering angle and $p_e(p_{e'})$ is the momentum of the incident (scattered) electron. From this equation the expression for the error in the momentum transfer can be obtained:

$$\begin{aligned} dq = & \frac{1}{q} [(p_e - p_{e'} \cos \theta)^2 dp_e^2 \\ & + (p_{e'}^2 - p_e p_{e'} \cos \theta)^2 (dp_{e'}/p_{e'})^2 \\ & + (p_e p_{e'} \sin \theta)^2 d\theta^2]^{1/2}. \end{aligned} \quad (2)$$

The first of these three contributions will normally be small compared to the other two, because of the well-defined beam momentum $dp_e/p_e \leq 10^{-4}$ [6]. The last term, which is due to the angular resolution, will in general dominate the resolution in q . The relationship of this third term to the second, which is due to the momentum resolution of the spectrometer, follows from the ratio

$$A = \frac{(p_{e'} - p_e \cos \theta)^2}{(p_e \sin \theta)^2}, \quad (3)$$

which is plotted in Fig. 1. Clearly, the angular resolution dominates almost all practical experimental conditions at the NIKHEF internal target facility ($\omega = p_e - p_{e'} \leq 350$ MeV, $20^\circ < \theta < 90^\circ$). A reasonable balance between the two contributions to dq is ensured by requiring that $dp_{e'}/p_{e'} \approx d\theta$. The resolution in q can then be approximated by

$$dq \approx p_{e'} d\theta. \quad (4)$$

For the desired resolution in the momentum transfer ($dq \leq 2$ MeV/c), an angular resolution of about 4 mrad is required. The momentum resolution $dp_{e'}/p_{e'}$ of the spectrometer should then be 4×10^{-3} for a central momentum of 500 MeV/c.

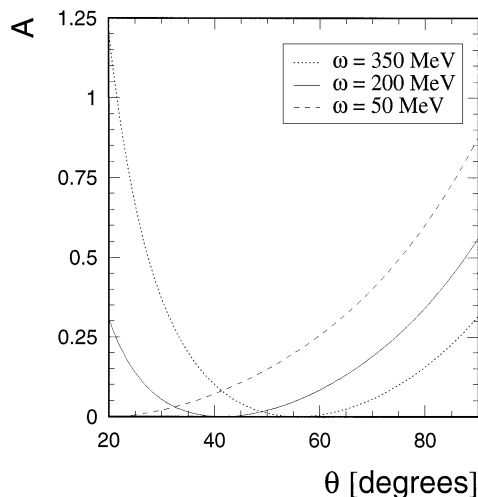


Fig. 1. The ratio A (see main text) as function of scattering angle θ , for three different values of the energy transfer ω .

This resolution in p_e (and hence, in ω) is sufficient for studies of few-body systems, the subjects of the experiments in the internal target hall at NIKHEF [3].

The momentum of a particle scattered into BigBite is obtained from the determination of the trajectory of the particle behind the magnet, and the constraint that the track originated at the target position. In order to determine completely the momentum of the scattered particle, at least two coordinates have to be determined at two different distances from the magnet. We use two sets of drift chambers for this purpose. To reduce the contribution to the multiple scattering two coordinates are measured simultaneously in each of these. One coordinate is determined from the drift time, the other (perpendicular) one from the charge induced on strips in the cathode plane. The trigger is provided by a scintillator detector. Particle identification is realized by means of a Cherenkov detector whose output can be added to the trigger logic to construct a more selective trigger.

3. Magnet design

The magnet is an H-shaped dipole with a gap of 25 cm. The entrance face is perpendicular to the central trajectory while the exit face has a pole face rotation of 5° . This enhances (reduces) the field integral for particles entering the upper (lower) region of the magnet, thereby making the dispersion more uniform across the acceptance of the spectrometer. At the nominal field of 0.92 T particles with momenta of 500 MeV/c that enter along the optical axis pass through the magnet along the central trajectory and are deflected over 25° . The length of this trajectory is 64 cm.

The magnet was designed in collaboration with the Budker Institute for Nuclear Physics in Novosibirsk. For the design we calculated the magnetic field in three dimensions using the computer code PROF1.¹ Low-carbon steel was used for both the yoke and polar pieces. The water-cooled coils

were made from hollow copper pipe with outer dimensions of $13.5 \times 15 \text{ mm}^2$ and a bore of 9.5 mm diameter. There are a total of ten pancakes, each with 36 turns. The coils are not parallel to the polar piece, but are slightly tilted such that the solid angle is not limited by the coils at the exit of the magnet. Excitation of 0.92 T requires a current of 518 A. Under normal operating conditions the temperature of the coils rises to about 55°C . Each pancake is equipped with a temperature controlled switch (clixon) to detect cooling problems. The current is supplied by an existing power supply² which can provide 920 A, stabilized to better than 1 part in 10^5 . The field is monitored with a Hall probe.

The magnet is placed on a support which can be rotated around a vertical line passing through the centre of the target. This support also carries the detector system and the rack containing the electronics. This limits the number and lengths of cables and thus reduces the effects of pick-up and of electromagnetic interference. The total mass of the spectrometer is about 20 tonne.

The support can be rotated using four heavy-duty air pads.³ The spectrometer is connected with the central pivot by a triangular guiding plate, thus fixing the centre of rotation. At the back of the support a dowel pin can be inserted into precisely positioned holes in the floor, which are located such that the spectrometer can be positioned at scattering angles between 25° and 90° at 5° intervals with a precision of better than 0.02° . The spectrometer is levelled and positioned at beam height with adjusting screws.

The target is located 1 m in front of the magnet. In order to shield the target area from the fringing field of the magnet a field clamp has been employed. Fig. 2 shows an artist's view of the spectrometer.

After assembly of the magnet the field was mapped out using a Hall probe. The measurements were done on a grid (dimensions: $40 \times 10 \text{ mm}^2$) in the median plane, and in two planes shifted 60 mm towards each polar piece. Fig. 3 shows the field measured along a horizontal line through the

¹ PROF1, PROF1-engineering systems GmbH, Darmstadt, Germany.

² Bruker-Physik AG, Karlsruhe, Germany.

³ AeroGo, type 4K27NHDL, Seattle, USA.

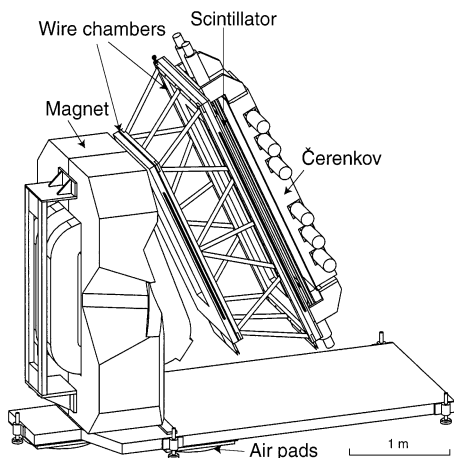


Fig. 2. Artist's view of the BigBite spectrometer, showing the magnet with its field clamp at the entrance, and the detector system consisting of two wire chamber packages, a scintillator, and a Cherenkov detector. The whole instrument is mounted on one platform and can be rotated around the target by means of an air pad system.

centre of the target. The experimental data (open circles) agree to within 1% with the PROFIL calculations, in the region where the field is greater than 1% of the central field.

4. Detector system

4.1. Requirements

The objectives of this spectrometer require the detector system to achieve a precise tracking of the particle, to discriminate between electrons and pions, and to deliver a precise (≤ 1 ns) timing signal for coincidence experiments.

The track parameters at the target can be calculated using the following approximate relations obtained from TRANSPORT calculations [7]:

$$\theta = 1.56x_1 - 0.81x_2, \quad (5)$$

$$\delta = -0.60x_1 + 0.47x_2, \quad (6)$$

$$y = 4.13y_1 - 3.10y_2 \quad (7)$$

$$\phi = -1.53y_1 + 1.50y_2. \quad (8)$$

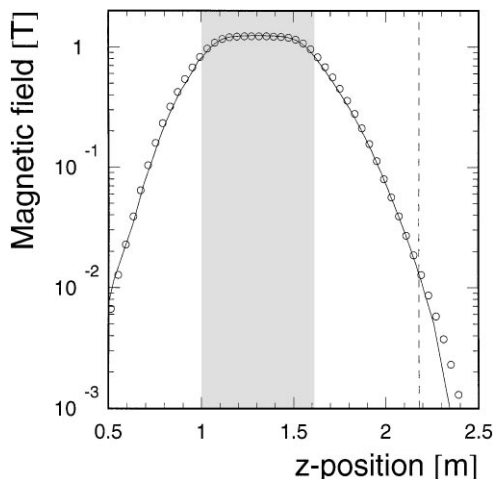


Fig. 3. The magnetic field of BigBite in the mid-plane of the magnet along a horizontal line through the target. The circles denote the measured field, the solid line is the result of a 3D-calculation. The target is situated at the origin $z = 0$, the shaded area indicates the region between the poles faces, and the dashed line gives the position of the first wire chamber.

The index i refers to the first and second drift chamber, x_i and y_i are the positions in mm of the track at the detector in the dispersive and non-dispersive directions, respectively; θ and ϕ are the angles at the target in these two directions in mrad; the quantities y and δ are the vertex position in mm, and the relative deviation from the central momentum (in %), respectively. For the dispersive direction the requirements for the position resolutions in the detector planes are thus determined by the energy resolution (4×10^{-3}), and for the non-dispersive direction by the precision of the vertex determination (1 mm). They are 0.5 and 0.2 mm, respectively. These accuracies are well within the capabilities of multi-wire drift chambers (MWDC), which have been chosen.

Discrimination between electrons and pions is achieved with an aerogel Cherenkov detector [8], while accurate timing is provided by a fast scintillator.

4.2. Cherenkov detector

The Cherenkov detector has an active area of 2100×500 mm² and a height of 240 mm. It

contains $2100 \times 500 \times 90 \text{ mm}^3$ Airglass⁴ aerogel (refractive index $n = 1.05$) as radiator. With this index the aerogel provides excellent efficiency for the detection of relativistic electrons while providing strong pion (and other particle) rejection [9], radiating for electrons of momentum greater than $1.58 \text{ MeV}/c$ while not radiating for pions of momentum less than $435 \text{ MeV}/c$. The light produced in the aerogel radiates into the $2100 \times 500 \times 150 \text{ mm}^3$ light-box region above the aerogel.

For simplicity of design and to achieve lower construction costs, a diffusely reflective light-box design was chosen over a focusing one. Millipore⁵ filter-paper type GSWP00010 is used as the diffuse reflector. This material has been shown to have an average reflectivity of 95% in the 350–450 nm region [10]. The diffusely reflected light is detected by twelve 5" Burle⁶ 8854 photomultiplier tubes which are spaced along two sides of the box above the aerogel; see Fig. 2.

The Cherenkov detector produces an average signal of 5.6 photoelectrons for an event caused by a singularly charged particle travelling with the speed of light. The signal is uniform to within one photoelectron over the entire active area of the detector.

Due to the good separation between zero and one photoelectron events provided by the Burle photomultiplier tubes, the detection efficiency ε can be estimated in the case that the threshold is below one photoelectron, using

$$\varepsilon = 1 - \exp(-N_e), \quad (9)$$

where N_e is the average number of photoelectrons [11]. When the threshold is more than one but less than two photoelectrons the efficiency is:

$$\varepsilon = 1 - (1 + N_e)\exp(-N_e). \quad (10)$$

Thus, the detector is estimated to have a detection efficiency for relativistic electrons of $(98.8 \pm 0.2)\%$ in the former case and $(93.4 \pm 0.2)\%$ in the latter.

The timing of the Cherenkov detector, measured with respect to the scintillator, has a sigma of 1.8 ns. The timing curve was calculated using a program designed to simulate diffusely reflective aerogel Cherenkov detectors [12], taking into account the size of the Cherenkov detector, the uncertainty of the transit time in each photomultiplier tube ($\sigma = 1.4 \text{ ns}$), and an estimate of the contribution from the scintillator ($\sigma = 0.5 \text{ ns}$). The simulated result agrees well with experiment, as is shown in Fig. 4

4.3. Scintillator

The scintillator is included in the detector package to contribute to the trigger and to provide information on the timing of the event. As is described in Section 5, the readout of the MWDCs is multiplexed, and already a modest position resolution in the scintillator can help resolve any uncertainties that may occur in the case of two almost simultaneous hits. Since the propagation time of the light through the slab can be determined precisely, and the scintillator is mounted close to one of the MWDC stacks, the location of the event on the surface of the latter can be reconstructed. For this reason we decided to use one single slab of scintillator material. Due to its size (2000×500

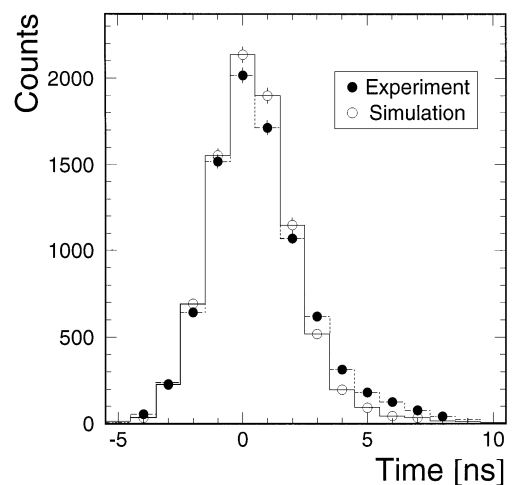


Fig. 4. Timing distribution in the Cherenkov detector relative to that in the scintillator.

⁴ Airglass, 5-245 00 Staffanstorp, Sweden.

⁵ Millipore Corporation, Bedford, MA 01730, USA.

⁶ Burle Industries, Lancaster, PA, USA.

$\times 10 \text{ mm}^3$), the greater attenuation length which NE110A⁷ provides (400 cm as opposed to 250 cm for NE102A) more than compensates for the slightly lower light output of the former.

The scintillator is viewed by four photomultipliers (EMI⁸ 9821S), two on each end (see Fig. 2). Each tube is optically connected by five 450 mm long rectangular (cross-section $50 \times 10 \text{ mm}^2$) light-guides, bent to fit the scintillator on one end and to form a $50 \times 50 \text{ mm}^2$ square on the other. This end matches well with the 60 mm diameter photocathode of the photomultiplier.

Electrons from a collimated ^{106}Ru -source (end-point energy 3.54 MeV) were directed through this scintillator towards a small trigger scintillator at 45 different positions on a 5×9 grid. Pulse height and timing spectra were measured for the four photomultipliers. From these spectra the light propagation properties of the scintillator were deduced. Fig. 5 shows the shift of the ADC-peak after pedestal subtraction, as a function of distance to the photomultiplier, from which an apparent attenuation length of 351 cm was deduced. Fig. 6 shows the timing difference between two facing photomultipliers, as a function of the pathlength difference from the source point to either of the two multiplier tubes. An effective refractive index of $n = 1.884$ is determined from these data. After completion of the spectrometer the position resolution of the scintillator was measured to be $\sigma = 6.9 \text{ cm}$ (see Fig. 7). The resolution of the TDC (1 ns per channel), contributes 5.3 cm to this value.

The detection efficiency of the BigBite scintillator was measured with cosmics. The scintillator was sandwiched between two small scintillators with areas of $500 \times 150 \text{ mm}^2$ and $50 \times 50 \text{ mm}^2$, respectively. The trigger was made by the coincidence between the two small scintillators. The efficiency was measured at 28 positions. Each single photomultiplier has a blind spot located near the light-guide of its neighbour caused by geometrical effects. The position and depth of these troughs in the efficiency were reproduced by a Monte Carlo

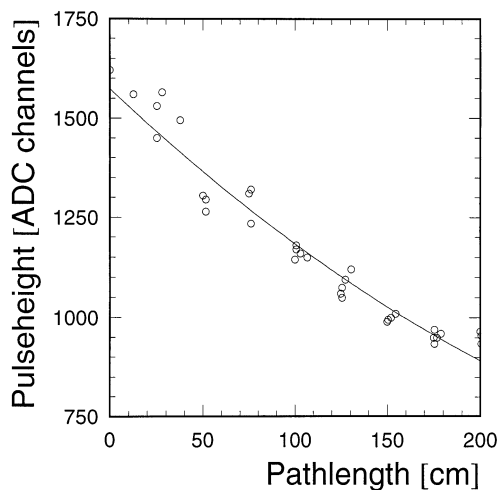


Fig. 5. The position of the ADC-peak in the scintillator after pedestal subtraction as a function of distance to the photomultiplier of the scintillator. The solid line is a fit which corresponds to an apparent attenuation length of 351 cm.

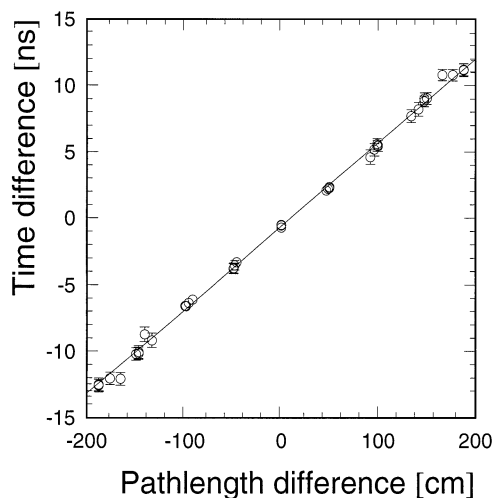


Fig. 6. Timing difference between two facing scintillator photomultipliers as a function of the pathlength difference from the source point to either of these PMTs. The straight line represents a fit from which an effective refractive index of $n = 1.884$ is determined.

simulation [13]. The average efficiency for detecting particles with at least one photomultiplier firing at each side of the scintillator was found to be $(99.86 \pm 0.09)\%$.

⁷ NE Technology Ltd., Beenham Reading, UK.

⁸ Electron tubes Ltd., Ruislip, UK.

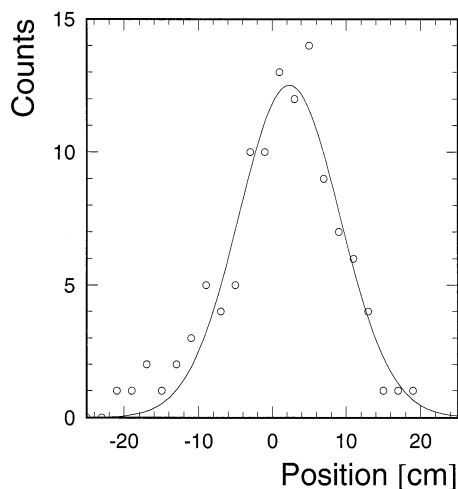


Fig. 7. Position resolution of the scintillator. The Gaussian fit has a width of $\sigma = 6.9$ cm.

4.4. Multi-wire drift chambers

A pair of MWDCs provides information on the track of the scattered electron. Each plane of the chamber measures two orthogonal coordinates to reduce the amount of material in the path of the particle. The x -coordinate is in the dispersive direction of the magnet and is obtained by the measurement of the drift time using the wire signals. The y -coordinate in the non-dispersive direction is determined by the charge distribution measured on the cathode. The cathode is divided into strips for this purpose.

4.4.1. Construction

Two drift chambers were built, each containing two anode wire planes, shifted half a pitch with respect to each other. This results in independent measurements at four different positions along the track. Three measurements are needed to solve the left–right ambiguity introduced by the drift time readout. Fig. 8 shows a schematic picture of one of these chambers.

The anode wires are made of gold-plated tungsten with a diameter of $20\ \mu\text{m}$. The wire pitch is 20 mm. Three field wires in a plane perpendicular to the anode plane are added between the anode wires to increase the detection efficiency at the

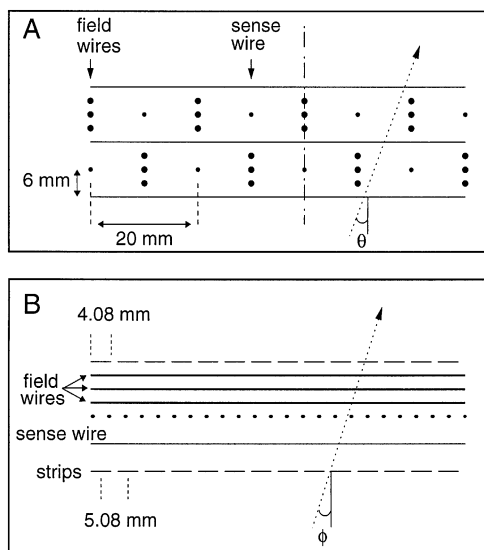


Fig. 8. Layout of the drift chambers with cathode strip readout. The panels A and B are views parallel and perpendicular to the sense wires, respectively. Dotted lines are projections of a track on these planes. The position of the cross-section shown in B is indicated in A by the dash–dotted line.

edges of the cell and to improve the separation of the cells.

The cathode plane between the two drift planes is made of gold-plated tungsten wires with a diameter of $100\ \mu\text{m}$ and a pitch of 1 mm. The outside cathode planes are made of a $75\ \mu\text{m}$ mylar foil with $0.2\ \mu\text{m}$ thick copper strips. The strips are 4.08 mm wide and are laid down at a pitch s_c of 5.08 mm. The anode–cathode distance is 6 mm.

The chambers, containing a mixture of argon and isobutane in a ratio of 3 : 1 by volume, are operated with a potential difference of +1850 V between the cathode planes (ground) and the sense wires. The detection efficiency at the edges of the cells could be improved by applying a negative voltage to the field wires. However, the electric field in the neighbourhood of the field wires would then leak into the other drift plane, since the cathode plane separating the two drift planes is made of wires and not of a homogeneously conducting foil. The electrons created in one plane could then be detected in the other. To prevent this the field wires are grounded.

Both chambers have the same configuration and differ only in size. The drift chambers have an active area of 1400×350 and 2000×500 mm², respectively. The two drift chambers are aligned on a rigid support frame, separated by 700 mm.

4.4.2. Dispersive direction

In a drift chamber, the time is measured between the passage of the charged particle and the detection of the avalanche on the anode wire. The reference time is given by the trigger detectors behind the second drift chamber. The uncertainty in this timing caused by differences in the time-of-flight for projectiles following different paths in the spectrometer is less than 1 ns, much smaller than the required accuracy in the determination of the drift time, which is about 12 ns. This value follows from the specified position resolution (500 μm) and the drift velocity close to the wire (40 μm/ns); see Fig. 9.

In order to convert the measured drift times to distances, a space–time relation, $r(t)$, was used approximated by a natural spline with a fixed number of equally spaced knots. A Monte Carlo technique was used, with a realistic theoretical $r(t)$, and realistic measurement errors. This showed that between five and seven fixed points suffice to

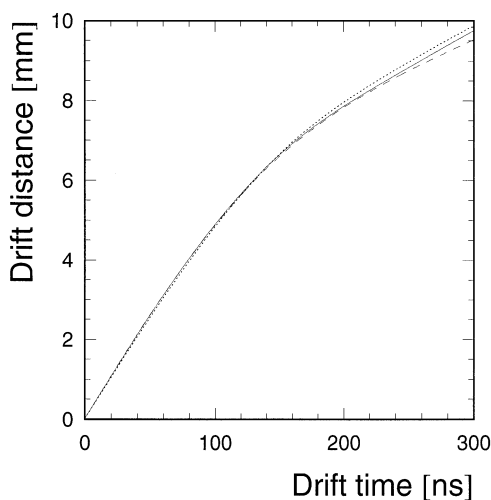


Fig. 9. Space–time relationship in the drift chamber calculated for a gas mixture of argon : isobutane = 3 : 1 (solid line). The dotted and dashed lines indicate the relation for gases with 7% less and more isobutane, respectively.

produce an interpolated $r(t)$ which is indistinguishable from the original in the entire time interval $[0, t_{\max}]$.

Starting from a theoretical estimate of $r(t)$ obtained by the MAGBOLTZ program [14], the positions of the knots were adjusted using a sample of about 10000 events to obtain the best linear fits for all tracks. Making use of the redundancy provided by the four planes the knots can be optimized in turn, thus speeding up the convergence of the process.

4.4.3. Non-dispersive direction

The partial avalanche caused by a single primary electron is located within approximately 10 μm along the wire [15]. In the case of a track caused by a charged particle this implies that the length of the full avalanche is determined by the orientation of the track with respect to the wire.

The separation of the electrons and positive ions drifting in opposite direction from this avalanche causes induced negative charges on the anode and positive charges on the cathode. From the distribution of the induced charges on the cathode the position of the avalanche in the direction of the anode wire can be reconstructed with a typical resolution of 60–300 μm [16–19], using the signals on only three neighbouring strips [20]. The induced charge on the central strip is called Q_m , that on its left and right-hand neighbour Q_l and Q_r , respectively. Fig. 10 shows the ratio Q_l/Q_m versus Q_r/Q_m . The y-coordinate of the track along the wire is a function of the position in this distribution varying from $-0.5s_c$ on the top left to $+0.5s_c$ on the bottom right.

The position of the avalanche can be calculated using the centre of gravity formula

$$y = C \frac{Q_r - Q_l}{Q_l + Q_r + Q_m}, \quad (11)$$

where C is a constant which depends only on the geometry of the cell and the layout of the cathode foil. This constant can be determined, like the space–time relation in Section 4.4.2, by optimizing the linear fits for a sample of tracks. The result ($C_{\text{obs}} = 1.61$) is close to the value which is obtained from the calculations shown in Fig. 10 ($C_{\text{calc}} = 1.59$).

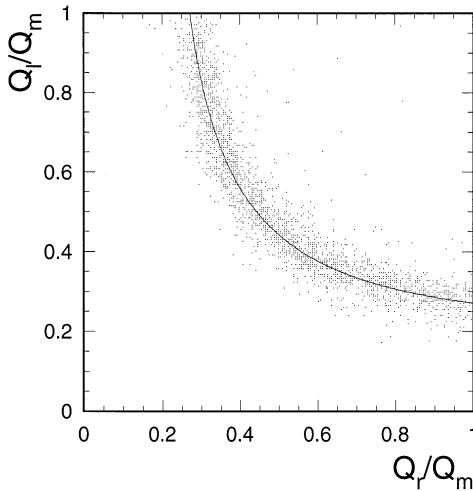


Fig. 10. Correlation plot of the ratio Q_l/Q_m plotted versus Q_r/Q_m , where Q_l , Q_m , and Q_r denote the charge induced in the left, central, and right cathode strips of the drift chamber. The solid line is the result of a calculation based in Ref. [18], using construction parameters and assuming a cross-talk of -12%.

After the cathode foils had been mounted on a frame, the position of the copper strips was measured with respect to the frame with a precision of $5\ \mu\text{m}$. It was found that the position of the strip varies with a period of 1 m and an amplitude of $100\ \mu\text{m}$. This error, and the error introduced by differences in amplification of the electronics, are corrected for in the off-line analysis of the data.

5. Data acquisition

In this section the main aspects of the triggering, and readout of the spectrometer are discussed. The triggering proceeds in three steps. The first (prompt trigger) level determines, on the basis of the scintillator and Cherenkov signals, whether a particle with the right properties has passed through the detector. This trigger can be transformed into a second trigger, called arm trigger (ATR), which starts the data acquisition modules. These will store their results in a memory, which will be read out on the receipt of the third trigger, the event trigger (ETR). This last trigger is gener-

ated by the coincidence detector, a circuit that determines a coincidence between one or more detector systems. The trivial case of one detector is provided to enable the measurement of singles spectra. If no ETR is received in a well-defined and tunable time interval, the data acquisition is aborted and the memories are cleared in preparation for the next event.

5.1. Triggers

The first-level trigger requires a pulse over threshold from both ends of the scintillator plus the presence or absence of a signal from the Cherenkov detector, in the case of an electron or non-electron trigger, respectively. The widths of the signals to this coincidence circuit are as small as is allowed by the differences in the propagation time of the light for events occurring at different positions. The dead time of this circuit is about 40 ns. The timing of the prompt signal is independent of the position of the event, and the trigger is available about 180 ns after the passage of the particle.

The prompt trigger is transformed into an ATR when not vetoed by either an external signal (e.g., from an auxiliary scintillator) or a busy signal. The ATR starts the acquisition modules, and the busy signal, which remains active for a preset time, waiting for the readout trigger from the coincidence detector. If this period elapses and no ETR has been received, the modules are cleared, after which the busy signal is taken away. If, on the other hand, an ETR arrives, the busy signal will be kept active until the data are read out from the hardware.

5.2. Drift chamber readout

The four drift chambers contain a total of 338 wires and 328 strips. The timing of the signals on the wires with respect to the ATR determines, together with the wire address, the coordinate in the dispersive direction. The address of the strip with the highest signal, and the pulse height on the neighbouring strips, determine the other coordinate. The large number of readout channels required and the low count rate expected suggest the use of a multiplexing scheme to reduce the former number.

5.2.1. Drift time measurement

The signals on the anode wires are individually amplified and discriminated. If any of these wires is hit, its address is coded by a priority encoder, and a pulse with a predetermined duration (1 μ s) is sent to an acquisition module in a VME-crate. The time of arrival of the pulse is stamped in this module with a resolution of 1.875 ns, and held until the trailing edge occurs, or the ATR appears. A single TDC channel is used to read out 16 wires. In a similar way, the time of arrival of the ATR signal is measured, using the same clock but in a different module. The drift time can thus be obtained by subtraction. A simple serial link between the VME-module and the front-ends at the wire chamber allows the setting of a threshold between 0.2 and 3.5 μ A, and the masking of any wire, e.g., to suppress hot wires.

5.2.2. Strip readout

For an accurate determination of the coordinate in the non-dispersive direction, which will be used to determine the ϕ angle and the vertex position of the scattered particle, the measurement of the charges induced on three neighbouring strips is required, see Section 4.4.3. Again, the signals on the strips are individually pre-amplified and shaped. Two shaping constants are used. The fast pulse ($t_{\text{rise}} = 43$ ns) drives a network which determines the strip with the highest signal on it. A set of analogue switches connects the slow output ($t_{\text{rise}} = 385$ ns), which is used to reduce the noise, of that and that of the two neighbouring channels to three ADCs [17]. The output from the central strip is connected to the analogue input of one ADC, and to the reference inputs of the remaining two. The inputs of the latter are connected to the left- and right-hand neighbour. The available data are thus the charge on the central strip Q_m and the ratio Q_l/Q_m and Q_r/Q_m .

This system is triggered by any event which causes a signal on two neighbouring strips, causing a dead time of 7.5 μ s which applies to all strips connected to the same set of three ADCs. We have introduced an extra circuit, the pre-trigger, to prevent the process from starting up when no prompt trigger is present. The singles count rate capability for the complete MWDC is thus

raised from about 27 kHz average, to 100–200 kHz. The prompt rate, however, should still be below 27 kHz.

6. Results

6.1. Efficiency

Three conditions should be fulfilled before a valid track can be determined in the detector package. First, a trigger is required. Second, for the determination of the x -coordinate, a hit on a wire in at least three MWDC planes is needed. The third x -coordinate is used to resolve the left–right ambiguity. Finally, two chambers must each have a plane in which a set of three consecutive strips with measurable signals is present to provide two measurements of the y -coordinate at different points along the track.

When BigBite is used as an electron spectrometer, the trigger is a coincidence between a scintillator and a Cherenkov signal. The threshold of the Cherenkov was between one and two photoelectrons. The efficiencies of these detectors are $(99.86 \pm 0.09)\%$ (see Section 4.3) and $(93.4 \pm 0.2)\%$ (see Section 4.2), respectively. The trigger efficiency is therefore $(93.3 \pm 0.2)\%$.

The efficiency of each wire plane was measured separately by counting the number of events with a missing plane in a sample of tracks which have crossed that plane with certainty. The average efficiency is $(99.0 \pm 0.5)\%$ per plane. This efficiency depends only weakly on the position in the drift cell as is shown in Fig. 11, but is slightly worse in the second plane of each chamber. This variation is attributed to the different location of these planes with respect to the flow of the gas. The flow rate through the two chambers is not the same, which explains the difference in the second planes of these MWDCs. A similar variation is observed in Section 6.2 for the space–time relation. At the edges of the cell, near the field wires, the efficiency in the second plane drops to about 97(98)%, for the first (second) chamber, respectively. This is probably due to extra electron attachment. The probability of determining at least three valid x -coordinates on the track is thus $(99.94 \pm 0.08)\%$.

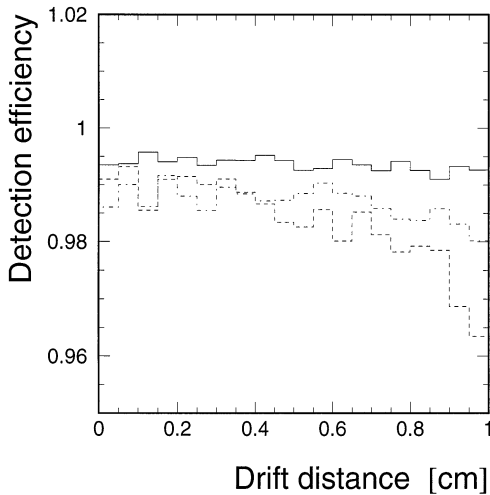


Fig. 11. Detection efficiency versus drift distance in a drift cell. The solid line is for the first plane of both chambers, the dashed and dash-dotted line for the second plane of the first and second chamber respectively.

The probability of finding valid signals on three consecutive strips in each strip plane when an avalanche occurs, was determined to be $(97.3 \pm 1.0)\%$ per plane. This number reflects the efficiency of the electronics chain used to read out the cathode strips and includes the inefficiency due to overflows in the ADCs (2%). The probability for the valid determination of at least one y -coordinate in each of the two chambers is therefore $(99.8 \pm 0.1)\%$. The total efficiency of the spectrometer is calculated from these three contributions to be $(93.2 \pm 0.2)\%$.

6.2. Resolutions

For each plane a separate space-time relation was needed. The space-time relation of the second plane of the first wirechamber, which showed the largest inefficiency in Fig. 11, deviated most (3%) from the average, probably also caused by the way the gas flow was organized (see Section 6.1). The difference cannot be explained by differences in construction or applied high voltage.

The resolution in the x -direction versus the drift distance is shown in Fig. 12. The degradation of the resolution near the sense wire is caused mainly by

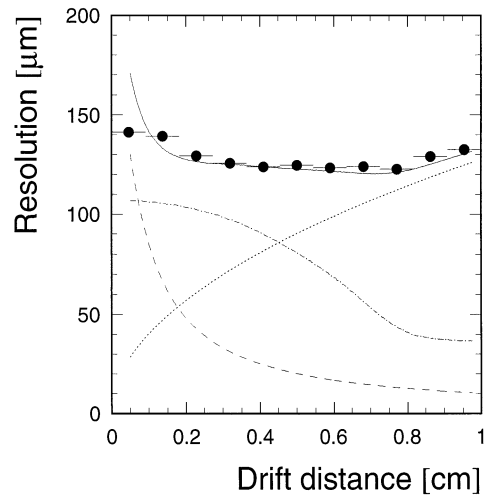


Fig. 12. Resolution (σ) in the dispersive direction versus the drift distance to the sense wire. The effects of clustering, diffusion, and the time resolution are indicated by the dashed, dotted, and dash-dotted line, respectively. The solid line is the sum of the three contributions.

the effect of clustering of the primary ionization. At larger distances from the sense wire the contribution of the diffusion of the primary electrons to the resolution becomes dominant. The third contribution is caused by the fixed time resolution of the electronics transformed to a space resolution by the space-time relation. These contributions and their sum are also indicated in Fig. 12.

Fig. 13 shows the resolution in the y -direction as a function of the position between strips. Zero indicates that the avalanche occurred precisely over the centre of a strip, while at ± 0.5 it was exactly between that strip and its left- or right-hand neighbour. The degradation of the resolution at larger distances from the centre of the strip is caused by the greater sensitivity to noise in this region and the fact that the discriminator circuit sometimes picks not the central strip but its neighbour. These effects were calculated using the equations from Ref. [18]. Noise was added to the three charge signals to reproduce the spread of the experimental points (see also Fig. 10). The calculated resolution was smoothed and is plotted in Fig. 13.

The timing resolution of the spectrometer was determined in a ${}^2\text{H}(e, e^2\text{H})$ experiment [21]. Fig. 14 shows the result after correction for

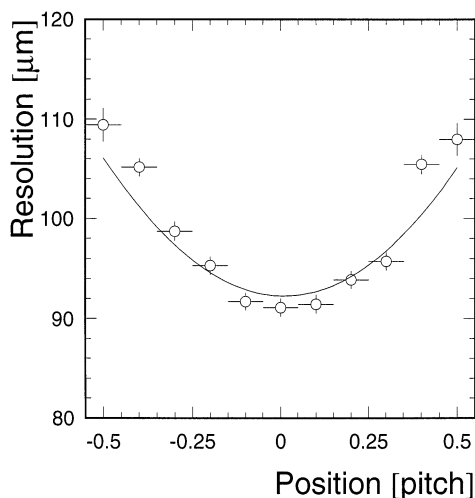


Fig. 13. Resolution (sigma) in the non-dispersive direction versus the distance to the central cathode strip. The position central above a strip has been assigned the value zero. The solid line is the calculated resolution as described in the main text.

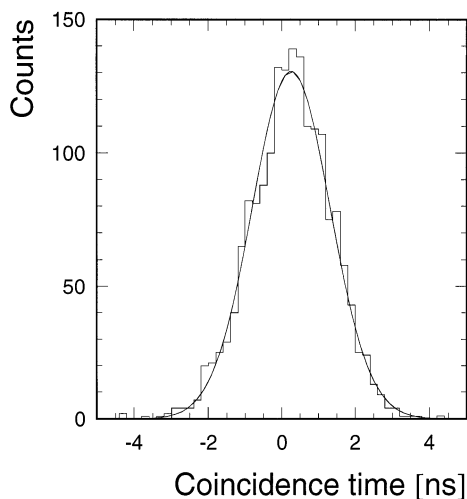


Fig. 14. Coincidence timing spectrum of the BigBite spectrometer with the Recoil detector. Corrections for walk and time-of-flight have been applied. The distribution has a width $\sigma = 1.06$ ns.

time-of-flight, walk in the discriminators, etc. The coincidence timing resolution determined from this plot is 1.06 ns, indicating a timing resolution for the BigBite spectrometer of $\sigma = 0.75$ ns.

Acknowledgements

The late Stan Popov was, with Kees de Jager, the leading force behind the collaboration between NIKHEF and BINP, which resulted amongst others in the construction of the magnet and the support for the BigBite spectrometer. Their effort is gratefully acknowledged. We would like to express our appreciation to T.A.W. Wijnen and C. Brouwer who developed the wire readout system. We thank R. Arink, H. Boer Rookhuizen, E. van de Born, J. Homma, A. Rietmeijer, H. Verkooijen, and A. Zwart for their efforts to complete this project. The design and construction of the Cherenkov detector was part of research supported by DOE Grant DE-FG05-87ER40364 and the University of Virginia. This work was supported in part by the Stichting voor Fundamenteel Onderzoek der Materie (FOM), which is financially supported by the Nederlandse Organisatie voor Wetenschappelijk Onderzoek (NWO).

References

- [1] Z.-L. Zhou et al., Nucl. Instr. and Meth. A 378 (1996) 40.
- [2] J. Stewart et al., Aspects of the design of the polarized H/D internal gas target storage cell for the HERMES experiment at HERA, in: Hans Paetz gen. Schieck, L. Sydow (Eds.), Int. Workshop on Polarized Beams and Polarized Gas Targets, World Scientific, 1996, pp. 408–412.
- [3] H.R. Poolman, et al. A polarized ^3He target for spin-dependent electron scattering at the AmPs storage ring, in: Hans Paetz gen. Schieck, L. Sydow (Eds.), Int. Workshop on Polarized beams and Polarized Gas Targets, World Scientific, 1996, pp 29–33.
- [4] R.M. Barnett et al., Phys. Rev. D 54 (1996) 1.
- [5] E. Passchier et al., Nucl. Instr. and Meth. A 387 (1997) 471.
- [6] P.K.A. de Witt Huberts, Nucl. Phys. A 553 (1993) 845c.
- [7] K.L. Brown et al., TRANSPORT, a computer program for designing charged particle beam transport systems, Technical Report CERN 80-04, CERN, 1980.
- [8] P. Dunn, Nucl. Instr. and Meth. 224 (1984) 106.
- [9] M. Anghinolfi et al., Nucl. Instr. and Meth. A 324 (1993) 191.
- [10] M. Benot et al., Nucl. Instr. and Meth. 154 (1978) 253.
- [11] P.J. Carlson, Nucl. Instr. and Meth. 192 (1982) 209.
- [12] D.W. Higinbotham, Nucl. Instr. and Meth., submitted.

- [13] T. Massam, GUIDE-7. a general program for evaluating the properties of scintillation and Cherenkov counter optical systems, Technical Report CERN 76-21, CERN, 1976, Revised 1982.
- [14] S.F. Biagi, Nucl. Instr. and Meth. A 283 (1989) 716.
- [15] G. Charpak et al., Nucl. Instr. and Meth. 148 (1978) 471.
- [16] G. Charpak et al., Nucl. Instr. and Meth. 167 (1979) 455.
- [17] H. van der Graaf et al., Nucl. Instr. and Meth. A 307 (1991) 220.
- [18] J. Chiba et al., Nucl. Instr. and Meth. 206 (1983) 451.
- [19] I. Endo et al., Nucl. Instr. and Meth. 188 (1981) 51.
- [20] E. Gatti et al., Nucl. Instr. and Meth. 163 (1979) 83.
- [21] M.J.M. van Sambeek, Ph.D. Thesis, Free University of Amsterdam, 1997, unpublished.